

## Status of the Belle II Pixel Detector

---

G. Giakoustidis,<sup>c,\*</sup> F. Abudinen,<sup>m</sup> K. Ackermann,<sup>m</sup> P. Ahlburg,<sup>c</sup> M. Albalawi,<sup>m</sup>  
 O. Alonso,<sup>a</sup> L. Andricsek,<sup>n</sup> R. Ayad,<sup>q</sup> V. Babu,<sup>f</sup> A. Baur,<sup>f</sup> F. Bernlochner,<sup>c</sup>  
 T. Bilka,<sup>o</sup> A. Bolz,<sup>f</sup> A. Bozek,<sup>i</sup> C. Camien,<sup>f</sup> A. Caldwell,<sup>m</sup> L. Cao,<sup>f</sup> V. Chekelian,<sup>m</sup>  
 A. Dieguez,<sup>a</sup> J. Dingfelder,<sup>c</sup> Z. Doležal,<sup>o</sup> M. Fras,<sup>m</sup> A. Frey,<sup>e</sup> M. Gabriel,<sup>m</sup>  
 K. Gadow,<sup>f</sup> T. Gessler,<sup>d</sup> D. Getzkow,<sup>d</sup> L. Gioi,<sup>m</sup> D. Greenwald,<sup>l</sup> M. Heck,<sup>h</sup>  
 M. Hensel,<sup>n</sup> M. Hoek,<sup>j</sup> S. Huber,<sup>l</sup> J. Kandra,<sup>o</sup> P. Kapusta,<sup>i</sup> R. Karl,<sup>f</sup> J. Kehl,<sup>f</sup>  
 C. Kiesling,<sup>m</sup> B. Kisielewski,<sup>i</sup> D. Kittlinger,<sup>m</sup> D. Klose,<sup>n</sup> P. Kodyš,<sup>o</sup> C. Koffmane,<sup>n</sup>  
 I. Konorov,<sup>l</sup> M. Krein,<sup>d</sup> S. Krivokuca,<sup>n</sup> T. Kuhr,<sup>k</sup> S. Kurz,<sup>f</sup> P. Kvasnička,<sup>o</sup>  
 J. S. Lange,<sup>d</sup> K. Lautenbach,<sup>d</sup> U. Leis,<sup>m</sup> P. Leitl,<sup>m</sup> D. Levit,<sup>l</sup> G. Liemann,<sup>n</sup> Q. Liu,<sup>f</sup>  
 Z. Liu,<sup>b</sup> T. Lück,<sup>k</sup> C. Mariñas,<sup>r</sup> S. Mccarney,<sup>m</sup> H. G. Moser,<sup>m</sup> D. Moya,<sup>p</sup>  
 F. J. Müller,<sup>f</sup> F. Müller,<sup>m</sup> C. Niebuhr,<sup>f</sup> J. Ninkovic,<sup>n</sup> B. Paschen,<sup>c</sup> S. Paul,<sup>l</sup> I. Peric,<sup>h</sup>  
 D. Pitzl,<sup>f</sup> A. Rabusov,<sup>l</sup> M. Reif,<sup>m</sup> S. P. Reiter,<sup>d</sup> R. Richter,<sup>n</sup> M. Ritter,<sup>k</sup> M. Ritzert,<sup>g</sup>  
 J. G. Sanchez,<sup>p</sup> B. Scavino,<sup>j</sup> G. Schaller,<sup>n</sup> J. Schmitz,<sup>c</sup> M. Schnecke,<sup>n</sup>  
 F. Schopper,<sup>n</sup> H. Schreeck,<sup>e</sup> B. Schwenker,<sup>e</sup> M. Schwickardi,<sup>e</sup> R. Sedlmeyer,<sup>m</sup>  
 C. Sfienti,<sup>j</sup> F. Simon,<sup>m</sup> S. Skambraks,<sup>m</sup> J. Skorupa,<sup>m</sup> Y. Soloviev,<sup>f</sup> B. Spruck,<sup>j</sup>  
 S. Stefkova,<sup>f</sup> R. Stever,<sup>f</sup> E. Tafelmayer,<sup>n</sup> M. Takahashi,<sup>f</sup> I. Vila,<sup>p</sup> A. L. Virto,<sup>p</sup>  
 S. Vogt,<sup>m</sup> C. Wang,<sup>b</sup> P. Wieduwilt,<sup>e</sup> H. Windel,<sup>m</sup> H. Ye,<sup>f,e</sup> J. Zhao<sup>b</sup> and R. Žlebčík<sup>o</sup>

<sup>a</sup>University of Barcelona,

C/Marti Franques, 1., 08028-Barcelona, Spain

<sup>b</sup>Institute of High Energy Physics, CAS,

19B Yuquan Road, Shijingshan District, Beijing, China

<sup>c</sup>University of Bonn,

53115 Bonn, Germany

<sup>d</sup>Justus-Liebig-Universität Gießen,

35392 Gießen, Germany

<sup>e</sup>II. Physikalisches Institut, Georg-August-Universität Göttingen,

37073 Göttingen, Germany

<sup>f</sup>Deutsches Elektronen-Synchrotron,

22607 Hamburg, Germany

<sup>g</sup>Institute for Computer Engineering, Heidelberg University,

69117 Heidelberg, Germany

<sup>h</sup>Karlsruhe Institute of Technology,

Hermann-von-Helmholtz-Platz 1, 76344 Eggenstein-Leopoldshafen, Karlsruhe, Germany

<sup>i</sup>H. Niewodniczanski Institute of Nuclear Physics,

Krakow 31-342, Poland

---

\*Speaker

<sup>j</sup>Johannes Gutenberg University Mainz,  
55099 Mainz, Germany

<sup>k</sup>Ludwig Maximilians University,  
80539 Munich, Germany

<sup>l</sup>Technical University of Munich,  
Arcisstrasse 21, D-80333 Munich, Germany

<sup>m</sup>Max Planck Institute for Physics,  
D-80805 Munich, Germany

<sup>n</sup>Halbleiterlabor der Max-Planck-Gesellschaft,  
Otto-Hahn-Ring 6, D-81739 Munich, Germany

<sup>o</sup>Faculty of Mathematics and Physics, Charles University,  
121 16 Prague, Czech Republic

<sup>p</sup>Instituto de Fisica de Cantabria (CSIC-UC),  
Avd. de los Castros s/n, 39005 Santander, Spain

<sup>q</sup>Department of Physics, Faculty of Science, University of Tabuk,  
Tabuk 71451, Saudi Arabia

<sup>r</sup>IFIC (UVEG/CSIC), Edificio Institutos de Investigación Apartado de Correos 22085 E-46071 Valencia,  
Spain

E-mail: [giakoustidis@physik.uni-bonn.de](mailto:giakoustidis@physik.uni-bonn.de)

The Belle II experiment at the Super KEK B-factory (SuperKEKB) in Tsukuba, Japan, has been collecting  $e^+e^-$  collision data since March 2019. Operating at a record-breaking luminosity of up to  $4.7 \times 10^{34} \text{ cm}^{-2} \text{ s}^{-1}$ , data corresponding to  $424 \text{ fb}^{-1}$  has since been recorded. The Belle II Vertex Detector (VXD) is central to the Belle II detector and its physics program and plays a crucial role in reconstructing precise primary and decay vertices. It consists of the outer four-layer Silicon Vertex Detector (SVD) using double-sided silicon strips and the inner two-layer PiXel Detector (PXD) based on the Depleted P-channel Field Effect Transistor (DePFET) technology. The PXD DePFET structure combines signal generation and amplification within the pixels with a minimum pitch of  $(50 \times 55) \mu\text{m}^2$ . A high gain and a high Signal-to-Noise Ratio (SNR) allow thinning the pixels to  $75 \mu\text{m}$  while retaining a high pixel hit efficiency of about 99 % for the Belle II PXD. As a consequence, the material budget of the full detector is kept low at  $\approx 0.21\% \frac{X}{X_0}$  per layer in the acceptance region. This also includes contributions from the control, Analog-to-Digital Converter (ADC), and data processing Application Specific Integrated Circuits (ASICs) as well as from cooling and support structures.

This article presents the experience gained from four years of operating the PXD; the first full-scale detector employing the DePFET technology in High Energy Physics. Overall, The PXD performance has met the expectations. Operating in the intense SuperKEKB environment poses many challenges that will also be discussed. The current PXD system remains incomplete with only 20 out of 40 modules having been installed. A full replacement has been constructed and is currently in its final testing stage before it will be installed into Belle II during the ongoing long shutdown that will last throughout 2023.

12-16 December 2022

Santa Fe, New Mexico, USA

## 1. Introduction

The Belle II experiment, the successor of the Belle experiment, started taking data in spring 2019, aiming for precision measurements of heavy flavor physics at unprecedented luminosity. It is located at the SuperKEKB accelerator [1] at KEK<sup>1</sup> (Tsukuba, Japan). Illustrated in Figure 1, SuperKEKB is an asymmetric electron-positron collider. The energy of the electron beam (High Energy Ring or HER) is 7 GeV and the one for the positron (Low Energy Ring or LER) is 4 GeV. The design peak luminosity of  $6.5 \times 10^{35} \text{ cm}^{-2} \text{ s}^{-1}$  is 40 times that of its predecessor, KEKB. The centre of mass energy of the collisions is 10.58 GeV corresponding to the rest mass of the  $\Upsilon(4S)$  resonance.

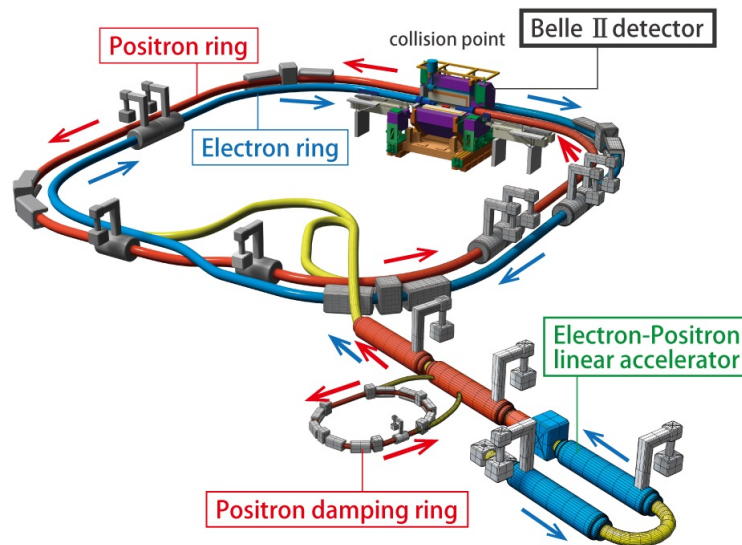


**Figure 1:** Illustration of the electron-positron collider at SuperKEKB.

The Belle II detector [2], as shown in Figure 2, is a general-purpose spectrometer consisting of various sub-detectors. From the outside inwards, the  $K_{\text{Long}}$ -Muon detector (KLM) is dedicated to  $K_L^0$  meson and muon detection. Surrounding the scintillator-crystal based Electromagnetic CaLorimeter (ECL) a superconducting solenoid coil provides a magnetic field of 1.5 T. The Time-Of-Propagation (TOP) in the barrel region and the Another Ring-Imaging CHerenkov (ARICH) counters in the forward end-cap serve the purpose of particle identification. The Central Drift Chamber (CDC), a wire chamber, is the main tracking device and it surrounds the Vertex Detector (VXD), which delivers an excellent vertex resolution necessary for the measurement of short lifetimes and flight paths. The VXD consists of a four-layer double-sided silicon strip detector, the Silicon Vertex Detector (SVD) [3] and the two-layer PiXel Detector (PXD).

<sup>1</sup>the High Energy Accelerator Research Organization

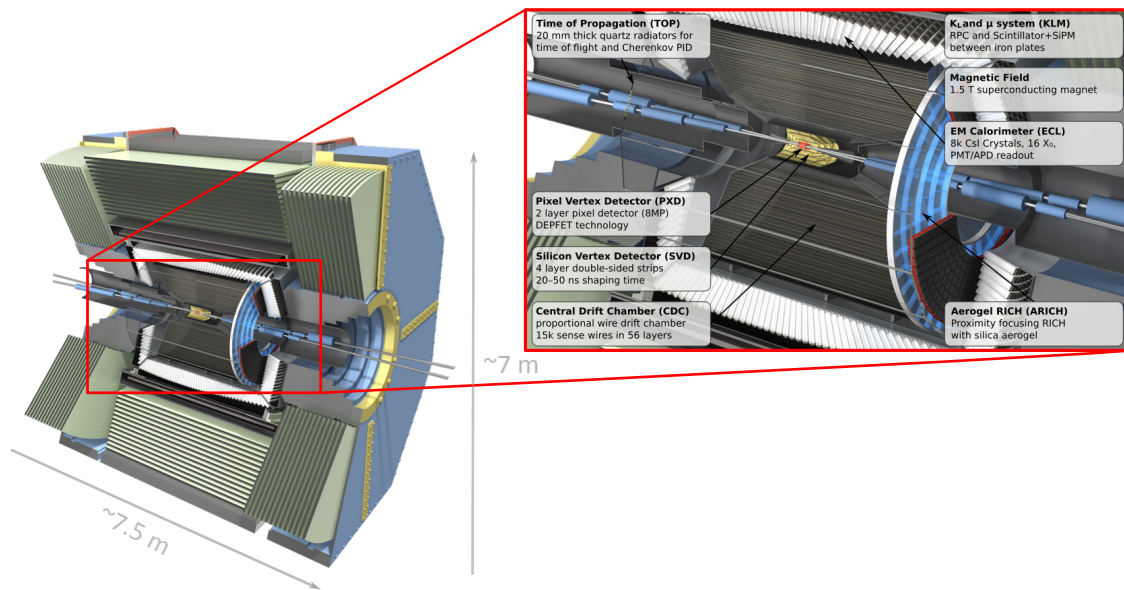


**Figure 2:** The Belle II detector with a zoomed-in view of the inner part.

## 2. The Belle II PXD

The PXD is the closest sub-detector to the Interaction Point (IP) and it is based on the DePFET (Depleted P-channel Field Effect Transistor) technology [4]. The PXD is the first full-scale detector employing the DePFET technology in High Energy Physics.

### 2.1 Detector design

The two layers of PXD are mounted on the 20-mm-diameter beam pipe at a radius of 14 mm and 22 mm from the IP, counting 8 and 12 ladders respectively as per design. A ladder is formed by two PXD modules coupled together with an edge-to-edge glue joint. Delays during the ladder gluing, the last production step, resulted in the incomplete installation of the outer layer with only two ladders along with the full inner layer. As depicted in Figure 3, the PXD module, with dimensions  $(1.5 \times 8.5) \text{ cm}^2$ , is composed of three main regions: (i) the active area, which hosts  $250 \times 768$  DePFET pixels with a varying pixel size of  $(50 \times 55 - 85) \mu\text{m}^2$ , offers an impact parameter better than  $15 \mu\text{m}$ , (ii) the balcony alongside the sensitive area, where six Switcher Application-Specific Integrated Circuits (ASICs) are located, responsible for steering the rolling shutter readout of the module with  $20 \mu\text{s}$  integration time, and (iii) the End-Of-Stave (EOS) region of the module, where 8 additional ASICs are bump-bonded, namely the Drain Current Digitizers (DCDs) and the Data Handling Processors (DHPs). The signals originating from the DePFET pixels are digitized in the DCDs through 8-bit Analog-to-Digital Converters (ADCs), resulting in a good energy resolution. The data are further handled and processed by the DHP, where data

reduction via zero suppression takes place as well. The module power consumption is summarized in Table 1. Since the rolling shutter mode is used for the readout and only the active pixels consume power, the power consumption of the DePFET sensor is very low.

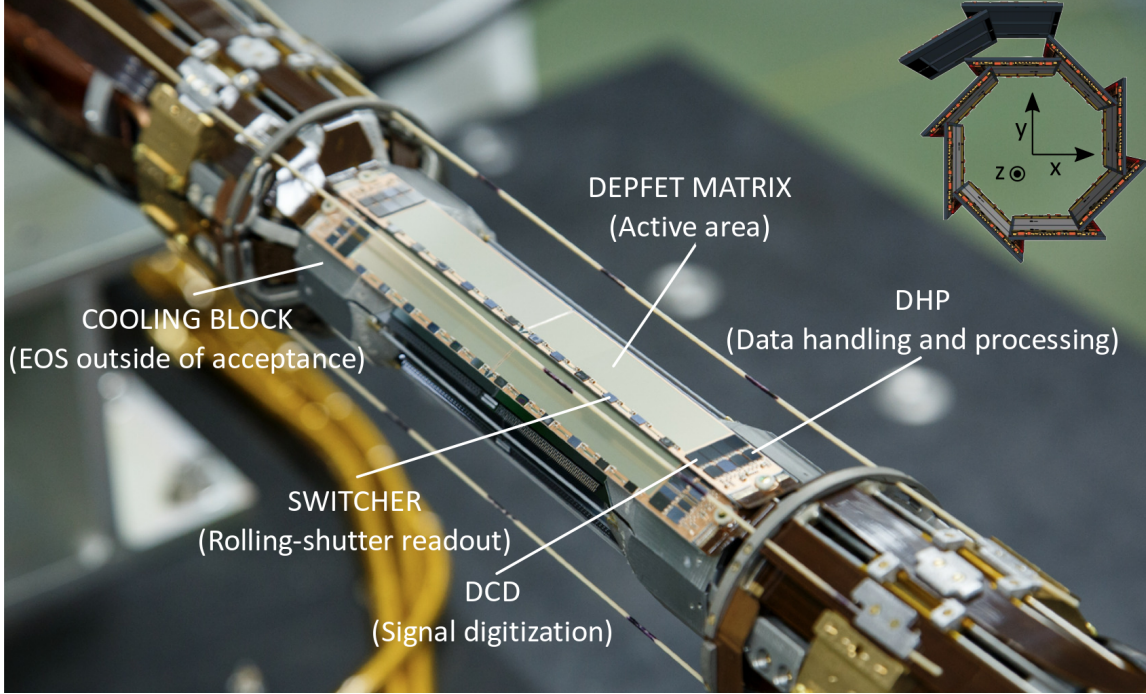


**Figure 3:** Picture of the PXD surrounding the beam pipe. The readout Application-Specific Integrated Circuits (ASICs) at the End-Of-Stave (EOS) are the components with the highest power consumption and heat dissipation, which necessitates active cooling. Thus, the EOS of the modules is mounted on the Support Cooling Block (SCB), which is cooled by a two-phase CO<sub>2</sub> cooling system. Active cooling is also used for the DePFET matrix and the Switcher ASICs by utilizing carbon tubes around the detector with N<sub>2</sub> flow. The module powering, the control signals and the data transmission are transferred via the Kapton cables at the outer side of the modules. The detector orientation relative to the Belle II coordinate system is illustrated in the upper right corner of the figure.

Device	Measured power
DHP	1.1 W
DCD	7.2 W
Switcher	0.2 W
DePFET sensor	0.5 W
Total	9 W

**Table 1:** Measured power consumption of a single PXD module [5].

The small capacitance of the internal gate ( $O(10 \text{ nF})$ ) provides low noise [4], and in combination with the high internal amplification of the signal in the sensor, this leads to high Signal-to-Noise Ratio (SNR). This allows for an extremely thin active area of  $75 \mu\text{m}$ , while the particle detection

efficiency is kept high. The EOS and the frame are kept at 525  $\mu\text{m}$  thickness, which makes the PXD module a mechanically self-supporting device. In addition, considering that the EOS is outside of the acceptance region, the material budget is kept very low at  $\approx 0.21\% \frac{X}{X_0}$  minimizing multiple scattering.

The DePFET pixels and all the ASICs are expected to be radiation tolerant at least until the end of the Belle II lifetime, which translates to radiation tolerance of  $\approx 200 \text{ kGy}$  in a time span of 10 years.

## 2.2 The DePFET technology and operating mode

The structure of a DePFET pixel and its equivalent circuit are shown in Figure 4a and 4b, respectively. On top of a depleted n-bulk a p-channel MOSFET is located, operated in saturation. The potential minimum for electrons is located in an additional deep n-well, called the internal gate, underneath the transistor channel. To accomplish bulk depletion the  $p^+$  backside implantation is biased with a negative voltage via a punch-through contact from the front-side, referred to as High Voltage (HV) [5]. The backside implant is enclosed in a  $p^+$  implant structure (guard-ring) to establish a gradual voltage drop to the cutting edge of the sensor. The electrons generated by ionizing radiation drift into the internal gate with a charge collection speed of a few nanoseconds, while the holes drift to the  $p^+$  backside contact and are removed from the volume. A  $p^+$  drift implantation surrounds the MOSFET structure to guide the drifting electrons to the internal gate.

The charges in the internal gate increase the source-drain current of the MOSFET constituting the detection signal. From the change in the source-drain current per unit charge the internal amplification  $g_q$  is derived, which can reach values up to  $750 \frac{\text{pA}}{e}$ . The charge collection takes place even if the MOSFET remains off, which allows building a low-power-consumption detector. The readout mechanism that is chosen for the PXD DePFET is the drain follower and it is performed by applying a negative voltage to the MOSFET gate. The internal gate needs to be cleared after the signal sampling to prepare for the next readout cycle. This is implemented by applying a high positive voltage pulse to the  $n^+$ -doped clear contact. Thus, the electrons drift to the clear contact and the internal gate is emptied. The deep p-well below the clear contact and the clear gate between the internal gate and the clear contact ensure that no electrons drift to the clear contact during the signal integration time. Due to space limitations, the long side of the matrix is divided into three regions and every region has its own MOSFET gate voltage and clear gate voltage line. Thus, the same negative voltage is applied for the MOSFET gate or the clear gate of all the pixels in a given region.

## 3. PXD optimization and operational evaluation

Every PXD module requires 23 different voltages to be operated, nine for the ASICs and 13 for the DePFET matrix biasing. Considering behavioral variance in ASICs and DePFET matrices as well, there is a broad margin of operational enhancement. Thus, optimization and calibration is essential to improve the overall sensitivity and performance of the detector.

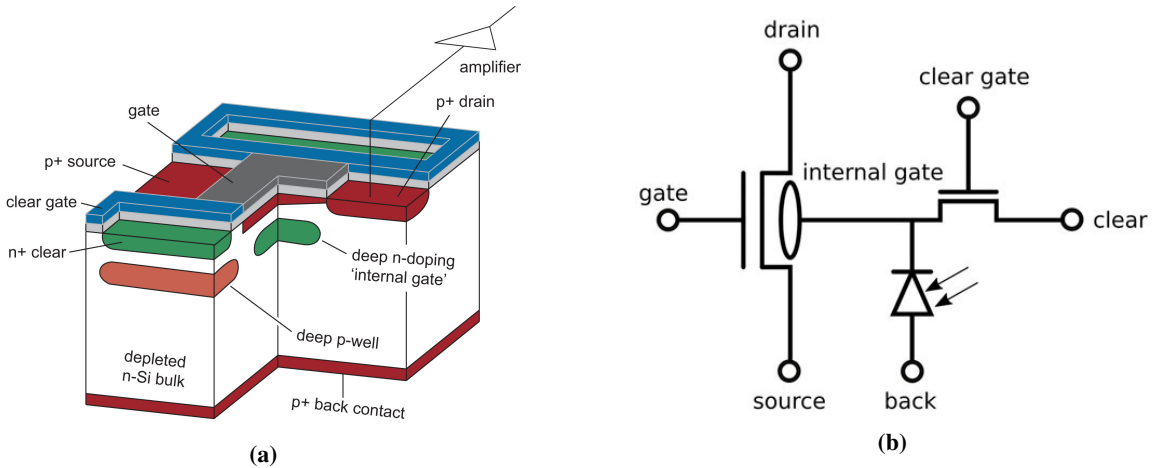


**Figure 4:** (a) Overview of the DePFET pixel cell [6], (b) Illustration of the DePFET equivalent circuit [7].

### 3.1 Optimization

One of the most important quantities of the PXD is the pedestal of the DePFET pixels, which is defined as the median value of measured current in the absence of traversing signal quanta. A typical pedestal value for a pixel is  $100 \mu\text{A}$ . The pedestals are measured for every pixel individually and after the readout the clean signal is obtained by subtracting the pedestals. The non-optimized (raw) pedestals of a PXD module are presented in Figure 5a as a raw pedestal map and raw pedestal distribution, respectively. All raw pedestal values need to lie at least within the dynamic range of the ADC to ensure a reliable signal measurement. Due to process variations within the DePFET sensor and the DCD the raw pedestal spread is large leading to underflow and overflow pedestal values for some pixels. Pedestal optimization is achieved by making use of two DCD features. The first one, namely the 2-bit DAC correction, compresses the pedestal distribution of the module by adding a predefined offset current to the input current on a pixel-by-pixel basis. In addition, utilizing the second feature of the DCD, the so-called Analog Common Mode Correction (ACMC), results in centering of the pedestal distribution. The ACMC is applied per four consecutive pixel rows. The combined effect on the raw pedestals is exhibited in Figure 5b. The pedestal spread is reduced significantly and the pedestal homogeneity along the module is increased. The raw pedestals after this optimization are referred to as corrected pedestals. The pedestal noise of a pixel is defined as the standard deviation of the pedestal measurements. The pedestal optimization being a complex routine is only used during the PXD module characterization, detector commissioning phase and on maintenance days. The pedestals are influenced by environmental changes, such as temperature, beam conditions and sensor biasing and consequently a regular update of the pedestal values is of great importance. Apart from the cases mentioned above for the pedestal optimization, the update of pedestal values is additionally performed at the end of every run at Belle II. The duration of a run at Belle II can vary from a couple of minutes to several hours.

The ADCs require an optimization as well, which is achieved by evaluating and correcting the ADC transfer curves based on inaccuracies and non-linearities. Communication errors between the DCD and the DHP should be minimized beforehand by configurable delay elements in the DHP. Although the ADC optimization is fully automated, it is multi-dimensional over large ranges and

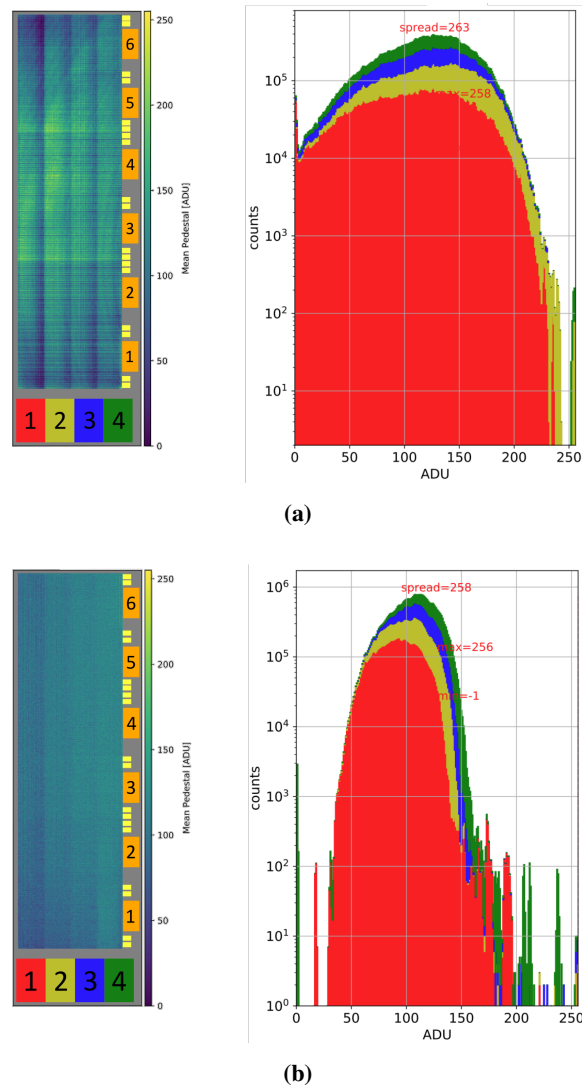


**Figure 5:** (a) Mapped median values of raw pedestals per pixel after 200 measurements, (b) Raw pedestal distribution of all pixels, (c) Mapped median values of corrected pedestals per pixel after 200 measurements, (d) Corrected pedestal distribution of all pixels. The pedestals of pixels digitized by the colored ASICs at the bottom of (a) and (c) constitute the pedestal distributions in (b) and (d) with the corresponding colors.

fine steps. This makes it very time-consuming and impossible to schedule during the maintenance days of the Belle II experiment. Thus, the ADCs of the modules need to be optimized before the integration of the PXD to the Belle II detector.

Another optimization routine is the so-called biasing optimization. The aim is to optimize the biasing voltages of the PXD sensors, so that the SNR is maximal and the pixel response homogeneous across the sensor. This routine requires test signals from a particle source and is so far done exclusively in the laboratory during characterization and commissioning.

### 3.2 Operational evaluation

Particles can traverse the detector non-vertically generating charge in several pixels (multi-pixel clusters). The multi-pixel cluster charge of a PXD module during data taking of the Belle II experiment is presented in Figure 6. The expected distribution is a sum of many Landau-Gaussian convoluted distributions, considering the energy loss of charged particles in the PXD and the detector energy resolution. The Most Probable Value (MPV) of this distribution is the wide peak slightly below 50 ADU. However, the most prominent peak is the one at  $\sim 15$  ADU, which is attributed to photon backgrounds and it is shortly discussed in Section 4.1. The MPVs are uniform over the sensor of a PXD module and the values for all the PXD modules lie within the range of 40 ADU to 50 ADU. Since the pedestal noise of the modules is  $< 1$  ADU, corresponding to less than  $\sim 200$  Equivalent Noise Charges (ENC) [8], the SNR of some modules is exceeding the 50 ADU. The SNR depends on the internal amplification of the DePFET sensors and the DCD gain, which can in principle differ from module to module. However, similar settings are achieved for all PXD modules in Belle II.

Regarding the detector performance, another important aspect, which depends on the SNR, is the hit efficiency. The hit efficiency of the PXD modules has been determined by using CDC and SVD tracking information, extrapolating these tracks to PXD looking for intersection points with pixel clusters. The hit efficiency is defined as:

$$\epsilon = \frac{n_{matched}}{n_{total}}, \quad (1)$$

where  $n_{matched}$  represents the number of tracks which have an associated cluster hit and  $n_{total}$  the total number of tracks. The comparison between data and Monte Carlo (MC) simulation along the z-axis is shown in Figure 7. The hit efficiency for the PXD modules is 96% on average. The simulation captures many features of the PXD already such as the dead regions of some modules due to beam loss events (shortly discussed in 4.1). These regions can have significantly lower hit efficiency compared to the nominally operating rows of  $\sim 99\%$ , marking the baseline at the plot. Another feature is the gap due to the glue joints of the ladders at  $\sim 1.5$  cm.

The transverse and longitudinal impact parameter resolution of the PXD was studied based on a small data sample collected in May 2019 and it was found to be  $(13.64 \pm 0.08) \mu\text{m}$  and  $(14.92 \pm 0.07) \mu\text{m}$ , respectively [9].

The PXD and SVD sub-detectors combined offer an average decay-time resolution of about 70 fs and 60 fs, respectively [10]. This resolution is improved by two times in comparison to Belle II predecessors, the Belle and BABAR experiments. The high precision measurements of  $D_0$  and  $D_+$  lifetimes presented in Figure 8 support this claim and the results are comparable to the world average.

## 4. Operational challenges

### 4.1 Beam backgrounds

The background sources at Belle II can be categorized in luminosity dependent backgrounds and beam-induced backgrounds. There are several different types of them [11], but the ones that

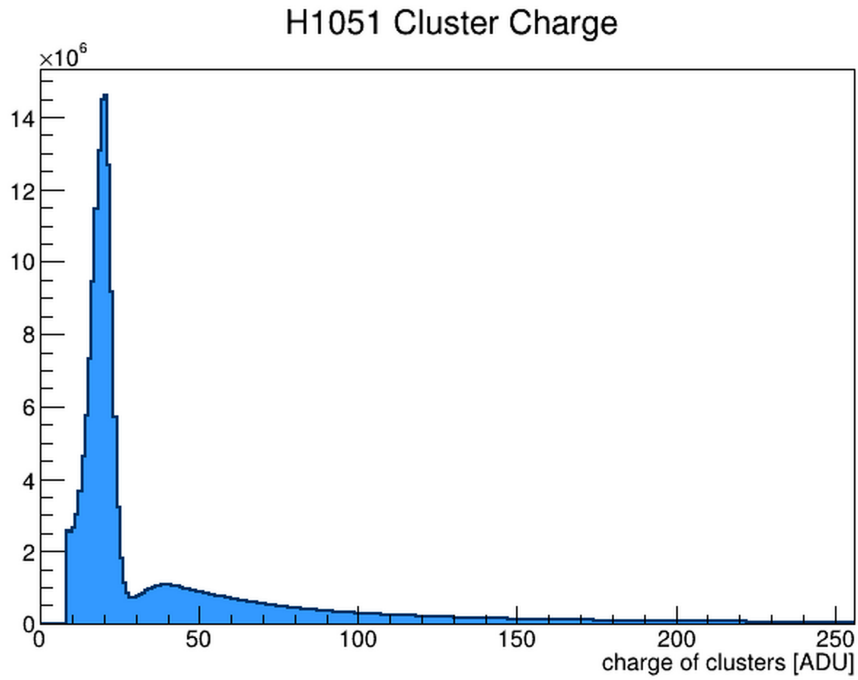


**Figure 6:** Cluster charge distribution of all cluster sizes for a PXD module in Belle II.

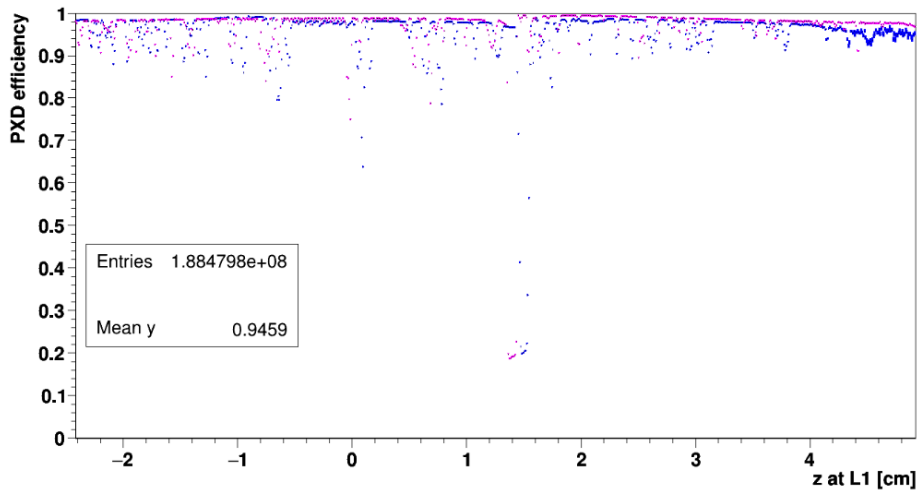


**Figure 7:** PXD hit efficiency as a function of  $z$ . Blue color is used to represent the calculated hit efficiency based on muon-pair events from experiments 22 to 26 with data corresponding to  $195 \text{ fb}^{-1}$ . The pink color represents Monte Carlo data from experiment 22 with simulated data corresponding to  $127 \text{ fb}^{-1}$ . The mean hit efficiency based on data and simulation is 94.6 % and 96 %, respectively.

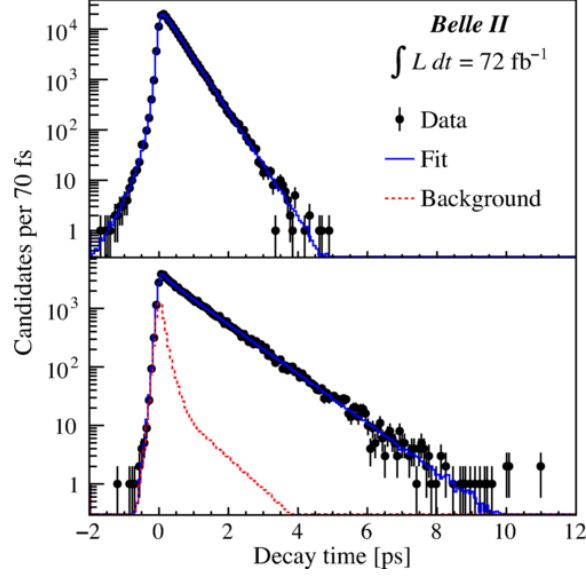


**Figure 8:** Decay-time distributions of  $D_0$  and  $D_+$  candidates in their respective signal regions with fit projections overlaid [10].

influence PXD the most are three and they are beam-induced: (i) the Synchrotron Radiation (SR), (ii) the beam injection, and (iii) the catastrophic beam losses.

When the positron or electron beams go through strong magnetic fields X-rays are emitted, which are referred to as direct SR. The region around the interaction point is designed in such a way that X-rays from direct SR do not hit the central part of the beam pipe. However, as already shown in Figure 6, X-ray photon background is observed on PXD, especially on the  $-x$  direction, which is attributed to SR being back-scattered (indirect SR) in the forward part of the beam pipe and in-homogeneously irradiating the PXD modules. A new beam pipe with additional gold plating and modified Ti part will be installed in 2023 to mitigate this effect. Due to this background source the clustering and the vertexing are degraded in the long run.

At SuperKEKB the so-called top-up injection scheme is used to keep the current of the beams stable by refilling the bunches in a continuous manner with a frequency of 25 Hz. This is necessary because the beam lifetime is short ( $O(10 \text{ min})$ ). However, the injected particles can lead to high particle background during the first milliseconds, because they do not enter the machine perfectly. A trigger veto is issued on the Belle II during beam injection to prevent the data readout.

During beam operation beam loss events might occur due to instabilities leading to radiation bursts and permanently damaging system components, such as beam collimators, or causing superconducting magnet quenches. Unfortunately, such events can damage the Switcher ASICs of the PXD as well. The damage effect is reflected to quadruple rows or even entire areas controlled by the damaged Switcher ASIC, making them inefficient or completely dead. The reason for this is yet to be found. Including an additional beam loss detector close to the IP and improving the emergency shutdown speed of the PXD from  $O(100 \text{ ms})$  to  $O(100 \mu\text{s})$  are some of the mitigation plans proposed by the accelerator and the Belle II side. The latter is being studied and tested.

## 4.2 Cumulative radiation effects

In principle, the PXD could suffer from both Total Ionizing Dose (TID) damage and displacement damage. According to previous studies [6], the expected displacement damage, based on the Non-Ionizing Energy Loss (NIEL) hypothesis, for the 10-year lifetime of the PXD is  $\approx 10^{13}$  MeV  $n_{\text{eq}}/\text{cm}^2$ , which is an order of magnitude less compared to the damage levels where type inversion starts. In addition, the noise increase at the expected levels is considered manageable. Therefore, displacement damage is not an issue for the PXD operation. The main radiation damage affecting the DePFET modules of the PXD is the TID damage. The integrated dose rate over time for all Layer-1 PXD modules in the forward (+z) direction is presented in Figure 9a. The TID is calculated as the integrated dose rate over time. Outside run periods the integrated dose rate exhibit plateaus. The integrated dose rate of PXD modules in the +x direction (modules 1.1.1, 1.2.1, 1.8.1) is higher, mostly because of Touschek backgrounds. This is expected according to simulations [12].

The TID damage affects the threshold voltage of the p-channel MOSFET, shifting it to more negative values. The gate voltages are adjusted to more negative values to keep the internal amplification constant. The oxide layer of the clear gate is affected as well by the TID damage and the clear-gate threshold voltage exhibits a similar shift. A parasitic channel between source and drain can be formed if the clear-gate potential is too negative and in case it is too positive charge losses can occur. Thus, the clear-gate voltage is adjusted towards negative voltages with increasing dose.

As explained in 3.1, pedestal optimization is crucial for increasing the pedestal homogeneity along the PXD module. Inhomogeneous radiation within the PXD modules in Belle II leads to inhomogeneous MOSFET gate threshold voltage shifts for the pixels and consequently the MOSFET gate voltage for every pixel needs a different adjustment. Unfortunately, as described in 2.2, the MOSFET gate voltage cannot be adjusted individually for every pixel and consequently the spread of the PXD module raw pedestal distribution increases. The increase of pedestal spread with irradiation is referred to as pedestal aging. Further pedestal aging result in raw pedestal values outside the dynamical range of the DCDs for some pixels and thus reducing the overall efficiency. Such pixels can become usable again after correcting the pedestals. However, pedestal aging affects the corrected pedestals as well, as shown in Figure 9b. This probably suggests that there is room for improvement in the pedestal optimization algorithm and it is currently under investigation.

During spring 2020 steadily increasing HV currents with increasing dose for different PXD modules were observed for the first time in Belle II. This effect was unforeseen and it is attributed to a sort between the guard-rings at the backside of the sensor. The effect is worse for some modules compared to others and this is confirmed by dedicated irradiation campaigns with PXD modules in the lab. Dedicated test-structures are also used in irradiation campaigns to study this effect in more detail. Since the PXD power supplies could initially supply only up to 1.3 mA for the HV channel, it was clear that once this limit is reached the supplied voltage to the HV contact would decrease and full depletion might not be reached. This leads to worse SNR and hit efficiency. Modifications of all the PXD power supplies to a 28 mA current limit for the HV channel were gradually performed over time to mitigate this effect.

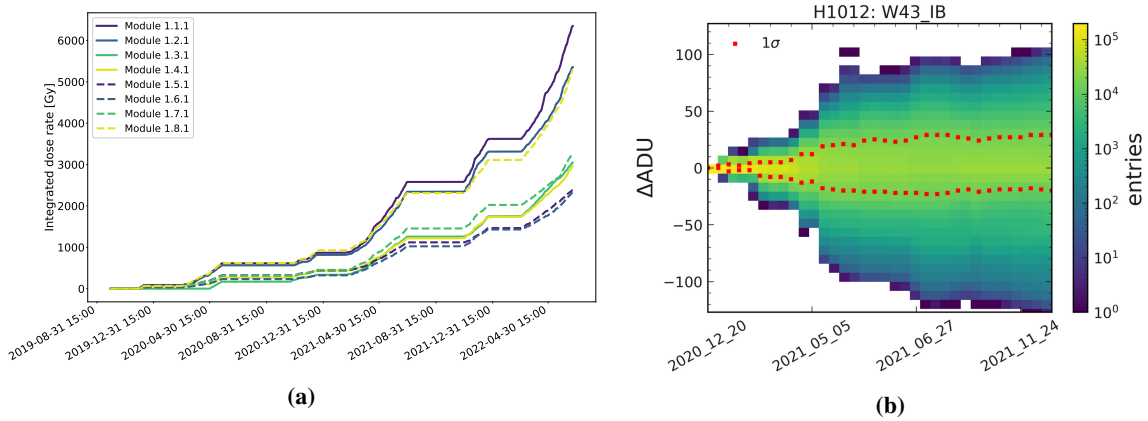


**Figure 9:** (a) Measured integrated dose rate for the IF modules [13], (b) Example of corrected pedestal spread increase with irradiation for a PXD module in Belle II [14].

## 5. Complete PXD (PXD2)

As mentioned in 2.1, the currently installed PXD is incomplete. In addition, it has experienced unforeseen damage due to beam losses, as discussed in 4.1, deteriorating significantly the overall hit efficiency by 2.5%. Although its performance is still within the nominal requirements, the expected increase in luminosity could deteriorate the tracking efficiency without the second layer in place. Thus, the installation of a complete PXD is planned during the Long Shutdown 1 (LS1). The LS1 started in July 2022 and it is expected to last until the fall/winter 2023.

The PXD2 is using the same design as PXD. The schedule from production to the final assembly of PXD2 with all the necessary tests has been long and it is still ongoing. Some important milestones reached are the sensor production, the module assembly, the module characterization at various collaborating institutes, the ladder assembly, the assembly of PXD2 in two Half-Shells (HSs) and the shipping of the latter to Deutsches Elektronen-Synchrotron (DESY) in Hamburg for the commissioning phase.

Since the PXD2 will be eventually integrated to the Belle II detector system, the commissioning at DESY Hamburg is one of the most critical phases for addressing issues, studying the detector properties, and making improvements if necessary. Thus, the setup at DESY Hamburg is equipped with a mock-up beam pipe and a cooling system for the PXD2 to imitate the inner part of the Belle II detector. In Figure 10 the PXD2 HS mounted on the mock-up beam pipe is depicted. Among others, conducted studies are the thermal tests of the mock-up beam pipe, gliding tests of the Support Cooling Block (SCB) relative to the mock-up beam pipe, alignment studies, mechanical stress tests of glue joints with mock-up ladders, ladder gliding tests on the SCB with mock-up and hot ladders, cooling stress tests, and extensive efficiency measurement with Sr<sup>90</sup> radioactive source.

## 6. Conclusion

PXD, the first DePFET-based detector in a full-scale High Energy Physics experiment, is crucial for vertexing in Belle II. Four years of PXD operation show that it met the performance expectations with longitudinal and transverse impact parameter resolution better than 15  $\mu\text{m}$  and hit efficiency in



**Figure 10:** Picture of the first PXD2 HS during the commissioning phase in DESY Hamburg.

nominally operated regions is  $\sim 99\%$ . Mitigation strategies for the operational challenges faced in the high-radiation environment of the SuperKEKB have been implemented or planned and further studies are ongoing for a better understanding. This will ensure a safer environment for PXD2, which is currently in its final testing stage and it will be installed into Belle II during the LS1.

### Acknowledgments

This work is supported by MEXT, WPI, and JSPS (Japan); MSMT, GAUK 404316 (Czech Republic), MSCA-RISE project JENNIFER-2 (EU grant 822070); Federal Ministry of Education and Research (BMBF, Germany); CIDEGENT/2018/020 of Generalitat Valenciana (Spain); National Natural Science Foundation of China (No. 11435013); and research grants S-1440-0321, S-0256-1438, and S-0280-1439 (University of Tabuk, KSA, Saudi Arabia).

### References

- [1] Y. Ohnishi, T. Abe, T. Adachi, K. Akai, Y. Arimoto, K. Ebihara et al., *Accelerator design at SuperKEKB*, *Progress of Theoretical and Experimental Physics* **2013** (2013) .
- [2] T. Abe, I. Adachi, K. Adamczyk, S. Ahn, H. Aihara, K. Akai et al., *Belle II Technical Design Report*, 2010. 10.48550/ARXIV.1011.0352.

- [3] K. Adamczyk, L. Aggarwal, H. Aihara, T. Aziz, V. Babu, S. Bacher et al., *The design, construction, operation and performance of the Belle II silicon vertex detector*, *Journal of Instrumentation* **17** (2022) P11042.
- [4] J. Kemmer and G. Lutz, *New detector concepts*, *Nuclear Instruments and Methods in Physics Research Section A: Accelerators, Spectrometers, Detectors and Associated Equipment* **253** (1987) 365.
- [5] F. Müller, *Characterization and optimization of the prototype DEPFET modules for the Belle II Pixel Vertex Detector*, July, 2017.
- [6] A. Ritter, L. Andricek, T. Kleinohl, C. Koffmane, F. Lütticke, C. Marinas et al., *Investigations on radiation hardness of DEPFET sensors for the Belle II detector*, *Nuclear Instruments and Methods in Physics Research Section A: Accelerators, Spectrometers, Detectors and Associated Equipment* **730** (2013) 79.
- [7] L. Andricek, A. Bähr, P. Lechner, J. Ninkovic, R. Richter, F. Schopper et al., *DePFET—Recent Developments and Future Prospects*, *Frontiers in Physics* **10** (2022) .
- [8] B. Wang, F. Abudinen, K. Ackermann, P. Ahlburg, M. Albalawi, O. Alonso et al., *Operational experience of the Belle II pixel detector*, *Nuclear Instruments and Methods in Physics Research Section A: Accelerators, Spectrometers, Detectors and Associated Equipment* **1032** (2022) 166631.
- [9] Q. Liu, F. Abudinen, K. Ackermann, P. Ahlburg, M. Albalawi, O. Alonso et al., “Operational Experience and Performance of the Belle II Pixel Detector.” 10.7566/JPSCP.34.010002.
- [10] BELLE II collaboration, *Precise Measurement of the  $D^0$  and  $D^+$  Lifetimes at Belle II*, *Phys. Rev. Lett.* **127** (2021) 211801.
- [11] A. Natochii, T.E. Browder, L. Cao, K. Kojima, D. Liventsev, F. Meier et al., *Beam background expectations for Belle II at SuperKEKB*, 2022. 10.48550/ARXIV.2203.05731.
- [12] A. Moll, *Comprehensive study of the background for the pixel vertex detector at belle ii*, July, 2015.
- [13] Y. Buch, *Total ionizing dose measurement of the Belle II pixel detector*, 2022.
- [14] M. Konstantinova, “Challenges of offset calibration in irradiated modules of the Pixel Vertex Detector at the Belle II experiment.”